Pacific Northwest
NATIONAL LABORATORY

PNNL-36556

# Programmable Catalyst Structures via Adsorbate-Induced Adatom Assembly

September 2024

Nicholas C. Nelson
Julia Nguyen
Zdenek Dohnalek
Micah P. Prange

U.S. DEPARTMENT OF ENERGY

Prepared for the U.S. Department of Energy
under Contract DE-AC05-76RL01830

## DISCLAIMER

This report was prepared as an account of work sponsored by an agency of the United States Government. Neither the United States Government nor any agency thereof, nor Battelle Memorial Institute, nor any of their employees, makes **any warranty, express or implied, or assumes any legal liability or responsibility for the accuracy, completeness, or usefulness of any information, apparatus, product, or process disclosed, or represents that its use would not infringe privately owned rights**. Reference herein to any specific commercial product, process, or service by trade name, trademark, manufacturer, or otherwise does not necessarily constitute or imply its endorsement, recommendation, or favoring by the United States Government or any agency thereof, or Battelle Memorial Institute. The views and opinions of authors expressed herein do not necessarily state or reflect those of the United States Government or any agency thereof.

PACIFIC NORTHWEST NATIONAL LABORATORY
*operated by*
BATTELLE
*for the*
UNITED STATES DEPARTMENT OF ENERGY
*under Contract DE-AC05-76RL01830*

**Printed in the United States of America**

**Available to DOE and DOE contractors from**
**the Office of Scientific and Technical Information,**
**P.O. Box 62, Oak Ridge, TN 37831-0062**
**www.osti.gov**
**ph: (865) 576-8401**
**fox: (865) 576-5728**
**email: reports@osti.gov**

**Available to the public from the National Technical Information Service**
**5301 Shawnee Rd., Alexandria, VA 22312**
**ph: (800) 553-NTIS (6847)**
**or (703) 605-6000**
**email: info@ntis.gov**
**Online ordering: http://www.ntis.gov**

PNNL-36556

# Programmable Catalyst Structures via Adsorbate-Induced Adatom Assembly

September 2024

Nicholas C. Nelson
Julia Nguyen
Zdenek Dohnalek
Micah P. Prange

Prepared for
the U.S. Department of Energy
under Contract DE-AC05-76RL01830

Pacific Northwest National Laboratory
Richland, Washington 99354

# Abstract

The electronic structure and geometric configuration of oxide-supported metal ions are important coordination properties that can be related to catalytic activity and stability. Herein, we interrogate the coordination environment of mononuclear Pd ions supported on ceria using CO adsorption, infrared vibrational spectroscopy, and DFT modeling. We observed the 15 h continuous co-evolution of a palladium- (2167 $cm^{-1}$) and cerium-carbonyl (2177 $cm^{-1}$) complex by monitoring the $\nu$(CO) infrared region. The slow CO adsorption kinetics were caused by the reactive ligand exchange between an oxygen atom of the support and the CO adsorbate to yield an oxygen vacancy and adsorbed $CO_2$. We hypothesize that the co-evolved cerium-carbonyl complex was formed upon CO adsorption at or adjacent to this oxygen vacancy. Our hypothesis was experimentally supported by a dramatic attenuation of the cerium carbonyl signal upon pre-adsorption of water through an apparent competitive adsorption mechanism. The attenuation was also accompanied by a 6 $cm^{-1}$ redshift of the palladium carbonyl band (2161 $cm^{-1}$) attributed to hydrogen bonding between the carbonyl and a nearby hydroxyl. Characteristic n(CO) stretch frequencies catalogued through CO adsorption onto single crystal ceria by Wöll et al.1 led us to index the cerium carbonyl to the {100} nanofacet of the polycrystalline ceria support. It follows from the observed co-evolution of the two carbonyl complexes that Pd was also adsorbed at the {100} nanofacet. Redeployment of a previously developed DFT model by Ivanova-Shor et al.2 featuring square-planar coordination of Pd2+ at the {100} nanofacet ($O_4Pd$) of a $Ce_{21}O_{42}$ nanoparticle model qualitatively reproduced several experimental observations.

# Acknowledgments

This research was supported by the Open Call Initiative, under the Laboratory Directed Research and Development (LDRD) Program at Pacific Northwest National Laboratory (PNNL). PNNL is a multi-program national laboratory operated for the U.S. Department of Energy (DOE) by Battelle Memorial Institute under Contract No. DE-AC05-76RL01830.

# Contents



# Figures

# 1.0 Introduction

Late-transition metals supported on oxides are a widely studied catalyst class owing to their industrial relevance.[3] The metals often exist in nanoparticle form for commercial applications due to practical reasons, such as achieving economic space-time-yields or meeting regulatory requirements over multiyear continuous operation;[4] however, exceptions do exist.[5,6] From an atomistic perspective, the study of nanoparticle catalysts presents considerable challenges due to the variety of structures these particles can assume and the creation of metal-oxide interfaces that are challenging to selectively examine.[7,8] Deploying the metal component as isolated atoms (i.e., atomically dispersed) offers a means to eliminate the structural heterogeneity inherent in nanoparticles and gain an understanding about the chemical, structural, and electronic properties of metals in physical contact with oxides.[9] Consequently, atomically dispersed metals can serve as a tool to differentiate the chemistry occurring on metal-support interfaces from those on metal surfaces.[10,11] However, the structural simplification provided by isolated atoms is constrained by the distribution of adsorption sites on the heterogenous support surface, a limitation that may be partially mitigated by low metal loadings.[12]

Infrared (IR) vibrational spectroscopy using probe molecules is a common method to indirectly infer the chemical, structural, and electronic properties of oxide-supported metal catalysts. This is achieved by observing the perturbations in the spectroscopic response of the probe (adsorbate) caused by the entity to which it is bound (adsorbent).[13,14] A variety of probe molecules are known to interrogate the quantity, strength, and type of acid, base, and defect sites present on oxide supports.[15-21] Certain probe molecules can also provide information about the reactivity of the sites to which they adsorb through temperature programmed desorption studies.[21,22] Furthermore, the combination of probe adsorption with isotopic labeling experiments can yield further insights into the structure of surface species and reaction mechanisms.[23] Metals are frequently examined by the adsorption of CO, NO, or ethylene.[14,24-30] Of these, CO is the most frequently used due to the sensitive response of the $\nu$(CO) stretch frequency to the oxidation state or local coordination of the metal to which it is bound. For linearly adsorbed CO bonded through the carbon atom, the formation of sigma or ionic bonds with a metal cation results in electron donation of the slightly antibonding 5s molecular orbital to the metal center, strengthening the CO bond and resulting in a blueshift of the $\nu$ (CO) stretch relative to the gas phase molecule.[26] In the presence of pi bonding, electron density is transferred into the $2\pi^*$ molecular orbital of CO, weakening the bond and causing a redshift relative to the gas phase. Both bonding modes can coexist, but the one that dominates is revealed through the absorption wavenumber making CO adsorption well-suited for distinguishing between local coordination environments of supported metal ions.

There have been numerous publications focused on the synthesis and characterization of atomically dispersed Pd (or Pd ions) supported on various oxides;[31-45] however, in several of these studies the CO probe IR spectra do not support the formation, or even partial formation, of atomically dispersed Pd.[38-45] Bands ranging from 2215 – 2130 $cm^{-1}$ are typically attributed to CO adsorption on Pd(II) ions, albeit there is a certain level of ambiguity with assignments at the lower wavenumber range since PdO nanoparticles also

show an adsorption band around 2140 $cm^{-1}$.[46] The groups of Bell and Klissurski et al.[31,32] used CO to probe 0.44 wt% Pd-H-ZSM-5 and observed two bands around 2221 $cm^{-1}$ and 2200 $cm^{-1}$ that were assigned to dicarbonyl adsorbed on Pd(III). This observation was recently confirmed for 1 wt% Pd/SSZ-13 and renamed to dicarbonyl on superelectrophillic Pd(II).[33] In addition to the dicarbonyl species observed for Pd-H-ZSM-5 and Pd/SSZ-13, other bands were observed at 2189, 2180, 2158, 2149, 2142, 2128, and 2110 $cm^{-1}$ attributed to CO adsorption on Pd ions in different oxidation states or coordination environments. There were also bands observed below 2000 $cm^{-1}$ that correspond to CO adsorption on zero-valent Pd (nanoparticles). The presence of nanoparticles introduces uncertainty to the assignment of bands between 2150 – 2100 $cm^{-1}$ region as they could be equally attributed to CO adsorption on few-atom clusters, which are undoubtedly present if isolated atoms and nanoparticles co-exist. For non-zeolite materials, CO adsorption onto 0.45 wt% and 0.97 wt% $Pd/Al_2O_3$ showed bands between 2160 – 2145 $cm^{-1}$ and 2135 – 2110 $cm^{-1}$ that were assigned to Pd(II) and Pd(I), respectively.[34,35] Adsorption of CO onto 1.5 wt% $Pd/WO_3$-$ZrO_2$ resulted in a band at 2184 $cm^{-1}$ attributed to Pd(II), which decreased in intensity with increasing temperature and gave rise to a band at 2145 $cm^{-1}$ that was attributed to Pd(I).[36] CO adsorption onto 1 wt% $Pd/CeO_2$ prepared through flame spray pyrolysis showed one band at 2143 $cm^{-1}$ attributed to Pd(II).[37] Finally, CO adsorption onto 0.01 wt% $Pd/TiO_2$ showed one band at 2136 $cm^{-1}$ attributed to atomically dispersed Pd.[11] The numerous aforementioned studies demonstrate the utility of CO to sensitively probe the electronic and geometric properties of Pd, while simultaneously demonstrating the uncertainty of relating bands to physical structure.

Herein, we probe the coordination environment of mononuclear Pd ions supported on ceria (0.034 wt.% Pd) using CO adsorption, IR spectroscopy, and DFT calculations. Our CO adsorption studies provided evidence that Pd atoms were adsorbed onto the {100} nanofacet of ceria. Exposure of the Pd atoms to CO resulted in reactive ligand exchange to yield an oxygen vacancy, adsorbed $CO_2$, and a palladium carbonyl with $\nu$(CO) stretch of 2167 $cm^{-1}$. The palladium carbonyl $\nu$(CO) stretch frequency depended on the hydroxyl coverage, as evidenced by a 6 $cm^{-1}$ redshift upon exposure to water vapor. Our results demonstrate the sensitivity of the CO probe molecule to detect changes in the local coordination of Pd caused by pretreatment conditions (e.g., exposure to water vapor) and to determine the Pd adsorption site onto the underlying ceria support.

## 2.0 Materials and Methods

Reagents. Tetraaminepalladium(II) nitrate (Sigma-Aldrich 377384), cerium(III) nitrate hexahydrate (Sigma-Aldrich 238538), and ammonium hydroxide (Sigma-Aldrich 221228) were used as received. Carbon monoxide (Matheson G1918775) was purified through submersion in liquid nitrogen to remove trace impurities (e.g., water, metal carbonyls, etc.) prior to each adsorption experiment. Oxygen (Matheson G2182140) was used as received. Water was obtained from a PURELAB flex system that provides ultrapure type I (18.2 MW.cm) water. The water was degassed through three cycles of freeze-pump-thaw.

Material Synthesis. Cerium(IV) oxide was synthesized through calcination of $Ce(NO_3)_3•6H_2O$ at 550 °C for 5 h in air with a 1 °C $min^{-1}$ ramp rate. Palladium (0.034 wt. %) was supported onto ceria using the strong electrostatic adsorption method.[47] Using a 250 mL Pyrex bottle, $CeO_2$ (2.0 g) was dispersed into 25 mL of water and 75 mL of 28-30 % $NH_3•H_2O$. It was then capped with parafilm. In a separate flask, 22 mL of 10 wt. % $Pd(NH_3)_4(NO_3)_2$ was added to 25 mL of 28-30 % $NH_3•H_2O$. This solution was introduced to the $CeO_2$ suspension at 0.5 mL $h^{-1}$ using a syringe pump while stirring at 500 rpm. Afterward, the Pyrex bottle containing the suspension was wrapped in aluminum foil and the parafilm removed. The Pyrex bottle was placed onto a hot plate to remove the solvent by evaporation under stirring (100 rpm). The temperature of the suspension was 60 – 70 °C during evaporation. The dried material was calcined in air at 400 °C for 4 h with a 2 °C $min^{-1}$ ramp rate. The material was outgassed for 4 h at 400 °C under turbo pump evacuation prior to the first CO adsorption experiment.

Fourier Transform Infrared Spectroscopy (IR). IR measurements were carried out on a Bruker Vertex 80 spectrometer equipped with a liquid nitrogen-cooled MCT detector operated at 4 $cm^{-1}$ resolution. Each spectrum was the average of 256 scans using a 2 mm aperture and 80 kHz scanner velocity. A Harrick Praying Mantis HVC-DRM-5 high temperature reaction chamber with ZnSe windows was used as the sample cell. The pressure in the IR cell could be controlled between < $10^{-3}$ and 10 Torr. We note there was an inherent leak in the IR cell (~33 mL) of ~0.05 mTorr $min^{-1}$ at 25 °C. The primary contaminants were nitrogen and water.

CO Adsorption. A typical CO adsorption experiment involved heating 0.034 wt.% $Pd/CeO_2$ under vacuum at 20 °C $min^{-1}$ to 400 °C for 2 h. Depending on the experiment, 3.9 Torr $O_2$ or $H_2O$ was introduced to the cell at 400 °C for 2 h. Afterward, the cell was evacuated for 0.5 h at 400 °C to remove $O_2$ or $H_2O$ and cooled to 25 °C. A background measurement was recorded at this time followed by admittance of 0.24 Torr CO.

X-Ray Photoelectron Spectroscopy (XPS). XPS measurements were performed using a Thermo Fisher NEXSA spectrometer with a 125 mm mean radius, full 180° hemispherical analyzer, and 128-channel detector. This system uses a focused monochromatic Al Kα X-ray (1486.7 eV) source for excitation and an electron emission angle of 60 degrees. The wide scan spectra were collected using a pass-energy of 200 eV with a step size of 0.5 eV. For the Ag 3d5/2 line, these conditions produced a FWHM of 1.95 eV. The binding energy (BE) scale is calibrated using the Cu 2p3/2 feature at 932.62 ± 0.05 eV and Au 4f7/2 at 83.96 ± 0.05 eV. Sample charging was corrected using the Ce 3d5/2 4f0 line at 916.7 eV.[48]

Inductively Coupled Plasma Optical Emission Spectroscopy (ICP-OES). A Perkin Elmer 7300DV ICP-OES with a cyclonic spray chamber and Meinhard nebulizer was used to determine the Pd content in the $Pd(NH_3)_4(NO_3)_2$ solution used during material synthesis. The Ar plasma was set at 1350 W. The system was calibrated with NIST traceable standards for Pd analyte and cross checked with independent NIST traceable standards.

Nitrogen physisorption. Nitrogen sorption was used to determine the surface area of Pd/CeO2 using a Quantachrome Instruments Quadrasorb SI surface area and pore size

analyzer. The sample was outgassed for 8 h at 300 °C and measurements were made in a 6 mm bulb using a 180 s thermal delay. The multipoint BET surface area of $Pd/CeO_2$ was 54 $m^2 g^{-1}$.

Peak Fitting. The IR bands within the range shown in the plots were fit using the lmfit Python library and the Voigt profile from the SciPy library. The Voigt profile was parameterized with the following constraints: a baseline modeled as a straight line with no variation allowed, an amplitude with no constraints, a center with a permissible shift of ± 1 $cm^{-1}$, a sigma (the Gaussian standard deviation) constrained between a minimum of 2.55 and a maximum of 6.37, and a gamma (the Lorentzian half-width at half-maximum) constrained between 0 and 2.8. These specific constraints were chosen to ensure a robust and accurate fit while accommodating the inherent variability and complexity of the spectral data.

Electronic structure calculations. To produce results comparable to previous literature, we attempted to use the same approximations as Nasluzov et al.[2] Our density functional theory calculations used the PW91 exchange-correlation[49] approximation augmented with onsite Hubbard corrections[50,51] of U-V = 4 eV for Ce f states. Simulations were performed at the Gamma point, and the plane wave basis set was determined by an energy cutoff of 415 eV. The projected augmented wave approach was used to soften the potentials.[52,53] Simulations were conducted using the VASP code.[54] All models were charge neutral and fully relaxed (internal coordinates of atoms and no constraints on spin polarization) in the final configurations.

# 3.0 Results and Discussion

## 3.1 DRIFTS Analysis of $CO/CeO_2$ and $CO/Pd/CeO_2$ Systems

We used wide-scan XPS analysis to determine the inorganic impurities that were present on the 0.034 wt. % $Pd/CeO_2$ surface. Documenting impurities can offer better reproducibility and explain anomalies between otherwise identical samples when studying dynamic systems. Figure S1 shows that the primary inorganic contaminant was fluorine (9 at. % relative to Ce and O), which was likely derived from the carbonate-fluoride mineral bastnäsite used by the supplier to prepare $Ce(NO_3)_3 \bullet 6H_2O$. Fluorine is a common ceria contaminant that substitutes oxygen atoms and results in an increased concentration of Ce(III) and modification of the O 2p valence band electronic structure.[55,56] The effects of F-impurity on the chemical properties of ceria have been seldom studied, and we could not find any studies related to its effect on supported metal atoms.[57] No attempts were made to remove the impurity.

We indirectly probed the local Pd coordination environment by adsorbing CO onto 0.034 wt.% $Pd/CeO_2$. The baseline experiment (reference state) involves heating $Pd/CeO_2$ under 3.9 Torr $O_2$ at 400 °C for 2 h followed by evacuation at the same temperature for 0.5 h and cooling to 25 °C before admittance of 0.24 Torr CO. Figure 1 shows IR spectra in the carbonyl region during exposure of $Pd/CeO_2$ to CO over 15 h and the corresponding time evolution of two carbonyl bands with $\nu$(CO) stretch frequencies at 2167 $cm^{-1}$ and 2177 $cm^{-1}$. We delineated between Ce and Pd carbonyls by exposing $CeO_2$ to CO. Like the experiment above, the $CeO_2$ support was treated in 3.9 Torr $O_2$ for 2 h, followed by evacuation at 400 °C for 0.5 h and cooling to 25 °C before admittance of 0.24 Torr CO. We observed several non-prominent bands for the 0.24 Torr $CO/CeO_2$ system that can be attributed to CO adsorption on low index facets of ceria (Figure S2).[58-61] The former experiment was repeated using 0.9 Torr CO, which resulted in one prominent $\nu$(CO) band at 2179 $cm^{-1}$ (Figure 2a). The control $CO/CeO_2$ experiments suggest the band observed at 2177 $cm^{-1}$ for $CO/Pd/CeO_2$ in Figure 1 was due to the formation of a cerium carbonyl complex, whereas the band at 2167 $cm^{-1}$ was due to the formation of a palladium carbonyl complex.

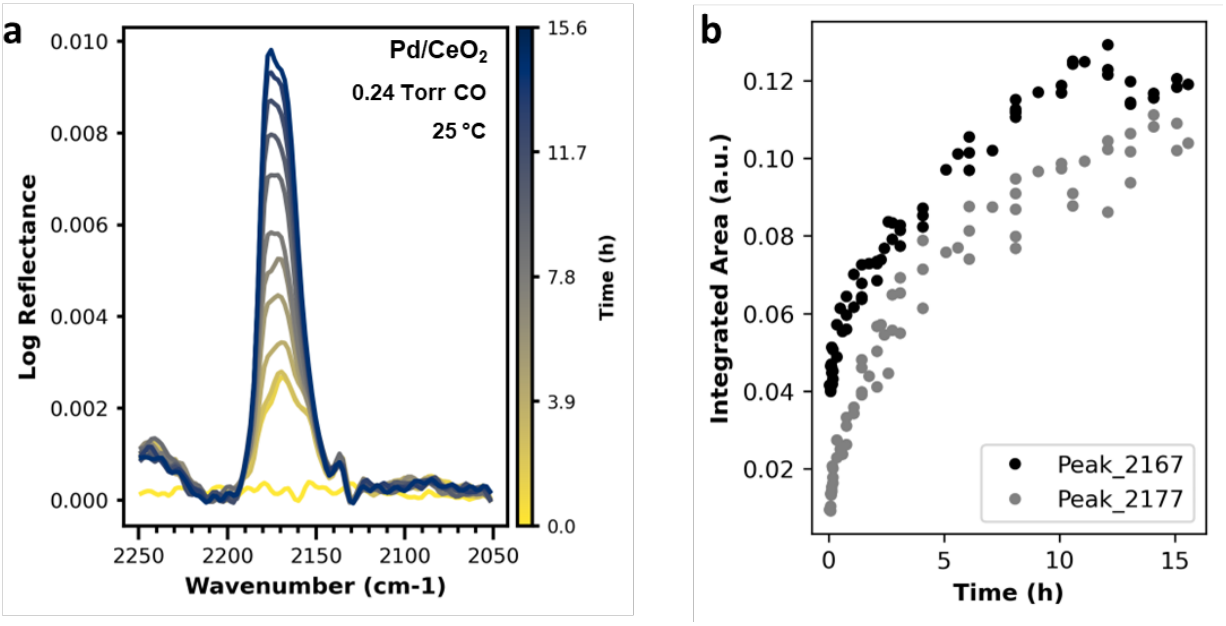


Figure 1. a) IR spectra n the carbonyl region during exposure of 0.034 wt% $Pd/CeO_2$ to 0.24 Torr CO at 25 °C following treatment in 3.9 Torr $O_2$ at 400 °C for 2 h. b.) Integrated area of the bands at 2167 $cm^{-1}$ and 2177 $cm^{-1}$ during contact with CO.

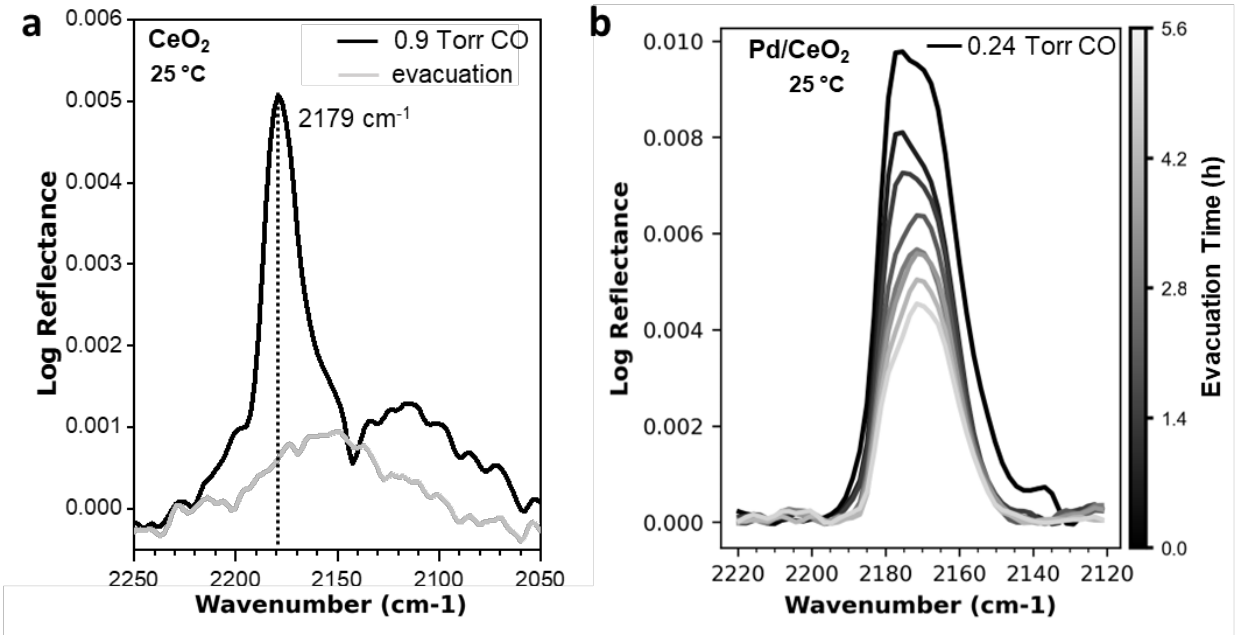


Figure 2. IR spectra in the carbonyl region a.) during exposure of $CeO_2$ to 0.9 Torr CO at 25 °C and evacuation at the same temperature. b.) during the evacuation of 0.034 wt.% $Pd/CeO_2$ at 25 °C following exposure to 0.24 Torr CO at the same temperature for 16 h (t = 0 h).

## 3.0 Results and Discussion

The assignment of the band at 2177 $cm^{-1}$ to cerium carbonyl for the $CO/Pd/CeO_2$ system seems straightforward given our observations for the $CO/CeO_2$ system. However, we note a few anomalies in the cerium carbonyl bands between the two systems. The cerium carbonyl band was less intense for $CO/CeO_2$ than $CO/Pd/CeO_2$ as evidenced by comparing the spectral regions of the two systems under 0.24 Torr CO (Figure 1a, S2). This discrepancy seems related to the fact that the two carbonyl bands in Figure 1 co-evolved, suggesting that palladium (carbonyl) imparts stability to, or creates, the cerium carbonyl, hence their co-evolution. The apparent stabilization manifested during the evacuation at 25 °C was evidenced by the immediate (< 30 s) disappearance of the cerium carbonyl band for the $CO/CeO_2$ system compared to its hours-long persistence for the $CO/Pd/CeO_2$ system (Figure 2). It is also worth noting the anomalously slow adsorption kinetics of CO onto Pd ions relative to the fast (< 10 min) adsorption saturation onto Pd nanoparticles and extended metal surfaces.[62] We reasonably speculate, given our collective knowledge of adsorption phenomena, that the slow adsorption kinetics were caused by the barrier to form a coordinatively unsaturated site on Pd through ligand exchange between support oxygen and a gas phase CO molecule (eq 1).$Pd\text{-}(O)_n + CO \rightarrow Pd\text{-}(O)_{n-1}\text{-}CO + O_{ad}$ (eq 1)

## 3.2 DRIFTS Analysis of $CO/Pd/CeO_2(OH)x$ System

The experiment in Figure 1 was followed by heating $Pd/CeO_2$ to 400 °C under evacuation and exposure to 3.9 Torr $O_2$ at the same temperature for 2 h. The $O_2$ was removed under evacuation for 0.5 h and 3.9 Torr $H_2O$ vapor was introduced at 400 °C for 2 h. The cell was then evacuated at the same temperature for 0.5 h and cooled to 25 °C under evacuation. Exposure of the sample to $H_2O$ vapor resulted in an increased surface concentration of hydroxyl groups (Figure S3). Figure 2 shows the IR spectra of the hydroxylated $Pd/CeO_2$ sample during 13 h exposure to 0.24 Torr CO at 25 °C. The primary $\nu$(CO) band for the hydroxylated $Pd/CeO_2$ was observed at 2161 $cm^{-1}$, a 6 $cm^{-1}$ redshift from the reference state shown in Figure 1. The redshift observed for the hydroxylated surface indicates a change in the local Pd coordination environment. We speculate that this change was caused by the formation of a hydroxyl that is either adjacent to, $Pd(O)_{n-1}(CO) + Ce(OH_{ad})$, or coordinated by, $Pd(O)_{n-2}(CO)(OH)$, an isolated palladium carbonyl, $Pd(O)_{n-1}(CO)$. Our hypothesis is supported by the fact that we purposely introduced hydroxyls and that the CO bond weakens ($\nu$(CO) redshifts) when the O-atom participates in hydrogen bonding.26 Similar to the reference state in Figure 1, the CO adsorption kinetics were slow on hydroxylated $Pd/CeO_2$, which suggests ligand change (eq 1) was necessary to form palladium carbonyl. We also note that the intensity of the cerium carbonyl band observed at 2175 $cm^{-1}$ was attenuated relative to the non-hydroxylated surface. The attenuation of cerium carbonyl on the hydroxylated ceria surface likely resulted from competitive adsorption between hydroxyl and carbonyl, the former being considerably more stable on ceria. The observed 6 $cm^{-1}$ redshift supports our hypothesis that competitive adsorption was the cause of the diminished cerium carbonyl.

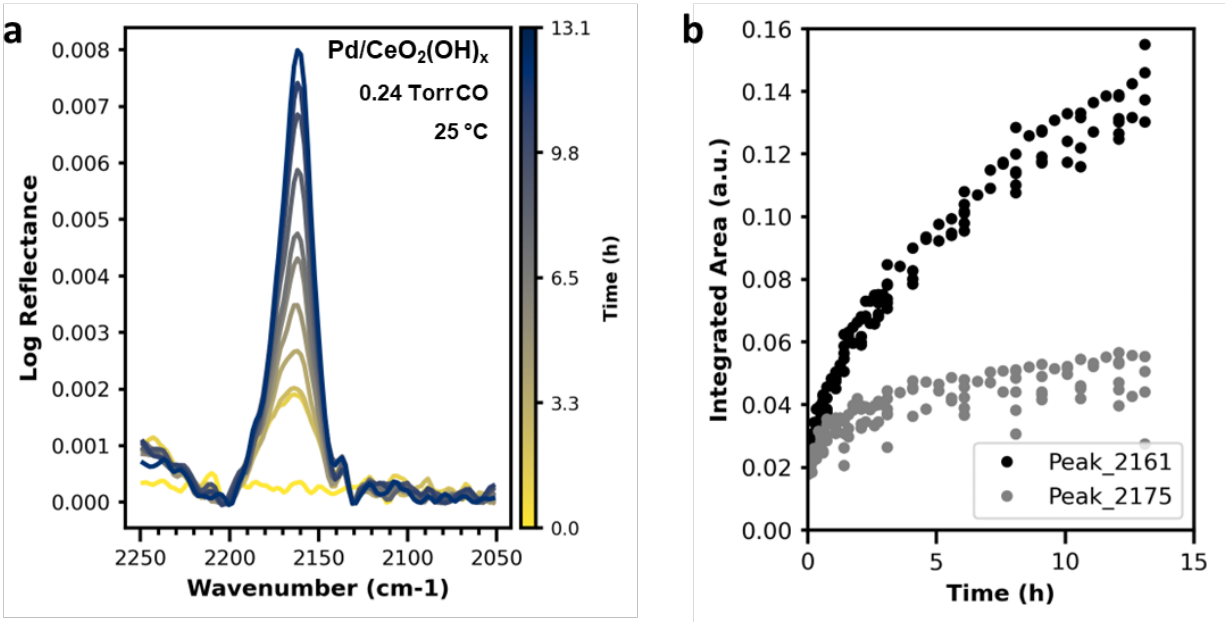


Figure 3. a.) IR spectra in the carbonyl region during exposure of Pd/$CeO_2$ to 0.24 Torr CO at 25 °C following treatment in 3.9 Torr $H_2O$ vapor at 400 °C for 2 h. b.) Integrated area of the bands at 2161 $cm^{-1}$ and 2175 $cm^{-1}$ during CO adsorption.

## 3.3 Literature IR for CO/sc-$CeO_2$ Systems

CO adsorption studies onto single crystal (sc) $CeO_2$ surfaces by Wöll and collaborators can be used to index the cerium carbonyl band observed here to a {100} nanofacet of the polycrystalline $CeO_2$ support.[58-61] The primary cerium-carbonyl band on the oxidized sc-$CeO_2$ (100) surface was reported at 2176 $cm^{-1}$, corresponding to CO adsorption onto undercoordinated (five-fold) $Ce^{4+}$ sites.[59] In comparison, the cerium-carbonyl band for the oxidized sc-$CeO_2$ (111) and sc-$CeO_2$ (110) surfaces were observed at 2154 $cm^{-1}$ and 2170 $cm^{-1}$, respectively.[58,60,61] The $\nu$(CO) band reported for the sc-$CeO_2$ (100) surface is similar to the CO/$CeO_2$ (2179 $cm^{-1}$) and CO/Pd/$CeO_2$ (2177 $cm^{-1}$) $\nu$(CO) band observed here. Moreover, the CO adsorption spectrum for sc-$CeO_2$ (100) showed two lower intensity $\nu$(CO) bands at 2168 $cm^{-1}$ and 2147 $cm^{-1}$ associated with CO adsorbed at different sites of the sc-$CeO_2$ (100) surface.[59] Likewise, the second derivative of Figure 2a also revealed two lower intensity $\nu$(CO) bands at 2173 $cm^{-1}$ and 2150 $cm^{-1}$ (Figure S4). The work by Wöll et al. and the observations made here for the CO/Pd/$CeO_2$ system provide support that the band at 2177 $cm^{-1}$ was caused by CO adsorption onto the {100} nanofacet of $CeO_2$, i.e., CO-$CeO_2${100}.

## 3.4 DFT Structure Model for the CO/Pd/$CeO_2$ System

A subtle, yet important point from the explicitly outlined observations in the results section is that the cerium and palladium carbonyl complexes were proximate to one another. Thus, the observance of $\nu$(CO) at 2177 $cm^{-1}$—indexed to CO adsorption onto $CeO_2${100} through studies of CO adsorption onto single crystal ceria—implies palladium atoms were also adsorbed on the {100} nanofacet of ceria. A literature search for density-functional

calculations of metal atom adsorption energies onto low-index facets of ceria does indeed identify the (100) facet as the preferred adsorption site for metal atoms. For instance, Konstantin Neyman's group has studied the adsorption energy of metal atoms onto ceria using density-functional calculations.[2,63-66] They use a cuboctahedral $Ce_{40}O_{80}$ or $Ce_{21}O_{42}$ nanoparticle that exposes small O-terminated {111} and {100} facets as a representative model of nanostructured $CeO_2$. They have shown that the {100} ceria nanofacet binds metal atoms more strongly than the corresponding edge atom in a 79-atom metal particle across 11 different metals.[64] Additionally, independent studies using a slab ceria model showed that the (100) surface was the most favorable low-index facet for metal atom adsorption.[66] Several recent experimental studies have also provided evidence that $CeO_2$-{100} nanofacets are preferred adsorption sites for late transition metal atoms.[67-69]

We deployed a recent local structural model developed by the Ivanova-Shor and Neyman groups that describes CO adsorption onto a square-planar Pd atom adsorbed at the {100} ceria nanofacet ($O_4Pd$) of a $Ce_{21}O_{42}$ nanoparticle (Figure 4a).[2] DFT calculations of the energetics for their model qualitatively reproduce several experimental results reported here. For instance, their model showed a weak CO binding energy of 0.13 eV to the $O_4Pd$ unit (Figure 4b, Pd-O distance of 2.05 Å) owing to the saturation of the Pd atom coordination sphere. The weak CO binding energy observed in their model is consistent with the relatively low palladium carbonyl signal observed at initial times (< 3 h) in Figures 1 and 3. Their CO/Pd/$Ce_{21}O_{42}$ model also showed that $O_4Pd$-CO complex could react with an oxygen-coordinating Pd to yield the $O_3Pd$-$CO_2$ complex with a room-temperature accessible barrier of 0.51 eV (Figure 4c). This oxidation reaction can also be characterized as a reactive ligand exchange like the one alluded to in eq. 1 and aligns well with the anomalously slow adsorption kinetics in Figures 1 and 3. We also observed the formation of carbonates (i.e., $CO_2$ adsorption onto ceria) during contact with CO (Figure S5); however, the undecorated ceria support was also active for CO oxidation (data not shown). Finally, they found that the removal of O-atom from $O_4Pd$ to form the $O_3Pd$ site resulted in notable increase of the CO binding energy (1.7 eV) caused by filling the Pd coordination sphere, i.e. $O_3Pd(CO)$. We calculated an apparent CO desorption energy of 0.7 eV using the Redhead equation (Figure S6).[49] We expect that the palladium carbonyl signal would have saturated within the 15 h observation period in Figure 1 if the Redhead energy reflected a barrierless adsorption energy. However, since the palladium carbonyl signal did not saturate, the Redhead energy strikes us as a notable increase in the apparent CO adsorption energy.

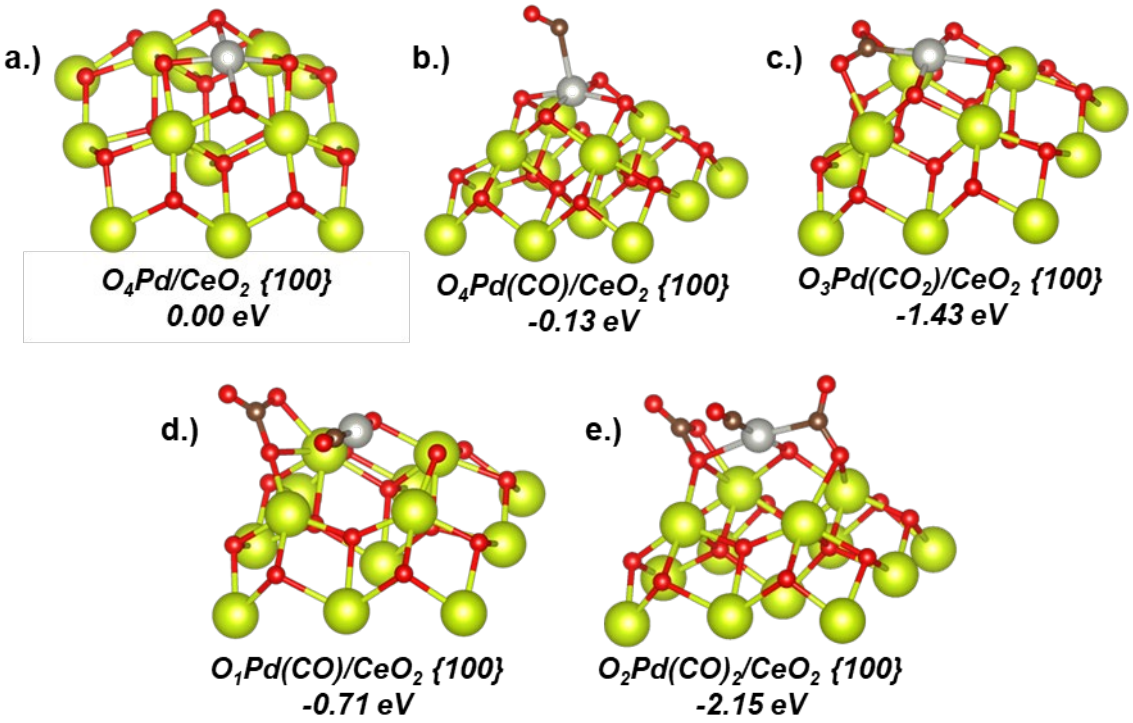


Figure 4. Structures from the model of Ref.2 showing a.) Pd adsorbed at the {100} nanofacet ($O_4Pd$), b.) a five-coordinate palladium carbonyl ($O_4PdCO$), c.) and a four-coordinate palladium carboxylate ($O_3PdCO_2$). Structures computed by us showing d.) a two-coordinate palladium carbonyl ($O_1PdCO$) with oxygen vacancy and adsorbed carbonate, e.) and a four-coordinate palladium dicarbonyl ($O_2Pd(CO)_2$). Pd atoms shown in silver, Ce in yellow, O in red, and C in brown. See the text for descriptions of the structures.

The qualitative similarity between the model introduced above and our experimental results led us to extend the model. We introduced an additional CO(g) to the $O_3Pd\text{-}CO_2$ complex and found a configuration where the bent $CO_2$ ligand of $O_3Pd\text{-}CO_2$ had retreated from the Pd center to coordinate another O atom from the Pd-conforming square to yield a $CO_3^{2-}$ group. The newly introduced CO(g) replaced the bent $CO_2$ ligand with a Pd-C distance of 1.84 Å. The O-atom opposite the newly adsorbed CO was retained at 2.10 Å, typical for Pd-O, while the remaining O atom retreated to 3.25 Å from the Pd center. This yielded a linear $O_1Pd\text{-}CO$ complex with adsorbed carbonate that was downhill by 0.71 eV (Figure 4d). The O atom used to form the adsorbed carbonate resulted in an oxygen vacancy ($V_O$) bridging two 5-coordinate Ce4+ cations. Intriguingly, this $V_O$ bridge site matches the one that Wöll et al.[1,59] associated with the 2176 $cm^{-1}$ $\nu$(CO) band on the sc-$CeO_2$(100) surface using a ceria slab model. However, addition of CO(g) to the linear $O_1Pd\text{-}CO$ complex with the bridging $V_O$ did not result in CO adsorption at the $V_O$, but rather bridge coordination of a Pd- and O-atom (Figure 4e). This preferred CO adsorption site largely derives from underlying differences between the slab and nanoparticle ceria models. For example, introduction of CO to $Ce_{21}O_{41}$ model with bridge $V_O$ did not result in CO adsorption at the $V_O$, but rather atop a $Ce^{4+}$ opposite the $V_O$ (Figure S7). Although there is a disagreement between the slab and nanoparticle ceria models regarding the favored CO adsorption site, both models point toward the 2177 $cm^{-1}$ band of the CO/Pd/$CeO_2$ system as belonging to a CO interacting with the ceria support. Our experimental results,

especially the attenuation of the signal by hydroxyl (Figure 3), also supports the computational finding. We also note that a $\nu$(CO) band at 2179 $cm^{-1}$ has been reported for CO adsorption onto atomically dispersed Pt on ceria.[68,70] The band was also assigned to CO adsorption onto surface Ce ions located in the direct vicinity of four-fold coordinated Pt ions.

The conversion from four- to two-coordinate Pd was accompanied by changes in the Pd electronic structure that point toward a weakening of the Pd-O binding. The linear Pd center adopted a more atomic-like electronic structure with less covalent bonding to the O atoms upon passage from the square planar coordination. This was reflected in the Pd Bader charge, which decreased from 0.86 in the square planar coordination to 0.33 in the linear configuration. At the same time, the projections of the densities of states (DOS) onto the Pd d and O p bands near the top of the valence band became less correlated upon conversion to the linear configuration (Figure S8). These electronic structure analyses are consistent with the occupied d-states of Pd hybridizing with neighboring O atoms to form covalent bonds that weaken as the number of O neighbors decreases. Moreover, the Pd center of the linear complex was 2.06 Å above the top layer of Ce surface atoms compared to only 0.81 Å for the square planar complex, consistent with weakened binding of Pd to the ceria support.

# 4.0 Conclusion

Rigorous examination of CO adsorption onto 0.034 wt.% $Pd/CeO_2$ using IR spectroscopy provided characteristic $\nu$(CO) stretch frequencies that can be used as a reference to detect induced changes in Pd ion coordination. The characteristic $\nu$(CO) stretch frequencies observed here, in combination with CO adsorption studies onto sc-$CeO_2$[58], points toward Pd adsorption onto the {100} nanofacet of polycrystalline $CeO_2$. A computational structural model developed previously,2 and co-opted by us, describing CO adsorption onto $O_4Pd/CeO_2$-{100} qualitatively reproduced several experimental observations. The throughline drawn between the aforementioned works and ours obliges us to conclude that Pd ions were apparently stabilized on the $CeO_2$-{100} nanofacet in square planar geometry. Exposure of the $O_4Pd/CeO_2$-{100} structural model to two CO molecules led to reactive ligand exchange to yield $O_1Pd(CO)/CeO_2$-{100} and adsorbed carbonate. The two-coordinate linear palladium carbonyl is likely to be more labile than the four-fold analog based on analysis of the DFT calculations, which suggests higher surface mobility. This research underscores the necessity of concentrating more characterization efforts on atom-adsorbate complexes to provide added utility to the atomically dispersed catalyst class.

# 5.0 References

1. Lustemberg, P. G.; Plessow, P. N.; Wang, Y.; Yang, C.; Nefedov, A.; Studt, F.; Wöll, C.; Ganduglia-Pirovano, M. V. Vibrational Frequencies of Cerium-Oxide-Bound CO: A Challenge for Conventional DFT Methods. Phys. Rev. Lett. 2020, 125, 256101.

2. Nasluzov, V. A.; Ivanova-Shor, E. A.; Shor, A. M.; Laletina, S. S.; Neyman, K. M. Adsorption and oxidation of CO on ceria nanoparticlese exposing single-atom Pd and Ag: A DFT Modelling. Materials [Online], 2021. https://mdpi-res.com/d_attachment/materials/materials-14-06888/article_deploy/materials-14-06888-v2.pdf?version=1637313693.

3. Allied Market Research - Metal Catalysts Market. https://www.alliedmarketresearch.com/metal-catalysts-market-A47250 (accessed 2024-03-20).

4. Datye, A. K.; Guo, H. Single atom catalysis poised to transition from an academic curiosity to an industrially relevant technology. Nat. Commun. 2021, 12, 895

5. Gao, F.; Mei, D.; Wang, Y.; Szanyi, J.; Peden, C. H. F. Selective catalytic reduction over Cu/SSZ-13: Linking homo- and heterogeneous catalysis. J. Am. Chem. Soc. 2017, 139, 4935-4942

6. Paolucci, C.; Khurana, I.; Parekh, A. A.; Li, S.; Shih, A. J.; Li, H.; Di Iorio, J. R.; Albarracin-Caballero, J. D.; Yezerets, A.; Miller, J. T.; Delgass, W. N.; Ribeiro, F. H.; Schneider, W. F.; Gounder, R. Dynamic multinuclear sites formed by mobilized copper ions in NOx selective catalytic reduction. Science 2017, 357, 898-903

7. Sun, G.; Sautet, P. Active site fluxional restructuring as a new paradigm in triggering reaction activity for nanocluster catalysis. Acc. Chem. Res. 2021, 54, 3841-3849

8. Neyman, K. M.; Kozlov, S. M. Quantifying interactions on interfaces between metal particles and oxide supports in catalytic nanomaterials. NPG Asia Mater. 2022, 14, 59

9. DeRita, L.; Resasco, J.; Dai, S.; Boubnov, A.; Thang, H. V.; Hoffman, A. S.; Ro, I.; Graham, G. W.; Bare, S. R.; Pacchioni, G.; Pan, X.; Christopher, P. Structural evolution of atomically dispersed Pt catalysts dictates reactivity. Nat. Mater. 2019, 18, 746-751

10. Nelson, N. C.; Nguyen, M.-T.; Glezakou, V.-A.; Rousseau, R.; Szanyi, J. Carboxyl intermediate formation via an in situ-generated metastable active site during water-gas shift catalysis. Nat. Catal. 2019, 2, 916-924

11. Nelson, N. C.; Chen, L.; Meira, D.; Kovarik, L.; Szanyi, J. In Situ Dispersion of Palladium on TiO2 During Reverse Water–Gas Shift Reaction: Formation of Atomically Dispersed Palladium. Angew. Chem. Int. Ed. 2020, 59, 17657-17663

12. Resasco, J.; DeRita, L.; Dai, S.; Chada, J. P.; Xu, M.; Yan, X.; Finzel, J.; Hanukovich, S.; Hoffman, A. S.; Graham, G. W.; Bare, S. R.; Pan, X.; Christopher, P. Uniformity is key in defining structure–function relationships for atomically dispersed metal catalysts: The case of $Pt/CeO_2$. J. Am. Chem. Soc. 2020, 142, 169-184

13. Lamberti, C.; Zecchina, A.; Groppo, E.; Bordiga, S. Probing the surfaces of heterogeneous catalysts by in situ IR spectroscopy. Chem. Soc. Rev. 2010, 39, 4951-5001

14. Groppo, E.; Rojas-Buzo, S.; Bordiga, S. The role of in situ/operando IR spectroscopy in unraveling adsorbate-induced structural changes in heterogeneous catalysis. Chem. Rev. 2023,

15. Thibault-Starzyk, F.; Maugé, F., Infrared Spectroscopy. In Characterization of Solid Materials and Heterogeneous Catalysts, 2012; pp 1-48.

16. Lercher, J. A.; Gründling, C.; Eder-Mirth, G. Infrared studies of the surface acidity of oxides and zeolites using adsorbed probe molecules. Catal. Today 1996, 27, 353-376

17. Knözinger, H.; Huber, S. IR spectroscopy of small and weakly interacting molecular probes for acidic and basic zeolites. J. Chem. Soc., Faraday Trans. 1998, 94, 2047-2059

18. Lavalley, J. C. Infrared spectrometric studies of the surface basicity of metal oxides and zeolites using adsorbed probe molecules. Catal. Today 1996, 27, 377-401

19. Montanari, T.; Bevilacqua, M.; Busca, G. Use of nitriles as probe molecules for the accessibility of the active sites and the detection of complex interactions in zeolites through IR spectroscopy. Appl. Catal. A - Gen. 2006, 307, 21-29

20. Hadjiivanov, K.; Knözinger, H. Characterization of vacant coordination sites of cations on the surfaces of oxides and zeolites using infrared spectroscopy of adsorbed probe molecules. Surf. Sci. 2009, 603, 1629-1636

21. Badlani, M.; Wachs, I. E. Methanol: A “smart” chemical probe molecule. Catal. Lett. 2001, 75, 137-149

22. Nelson, N. C.; Boote, B. W.; Naik, P.; Rossini, A. J.; Smith, E. A.; Slowing, I. I. Transfer hydrogenation over sodium-modified ceria: Enrichment of redox sites active for alcohol dehydrogenation. J. Catal. 2017, 346, 180-187

23. Lagunov, O.; Drenchev, N.; Chakarova, K.; Panayotov, D.; Hadjiivanov, K. Isotopic labelling in vibrational spectroscopy: A technique to decipher the structure of surface species. Top. Catal. 2017, 60, 1486-1495

24. Lansford, J. L.; Vlachos, D. G. Spectroscopic probe molecule selection using quantum theory, first-principles calculations, and machine learning. ACS Nano 2020, 14, 17295-17307

25. Lansford, J. L.; Vlachos, D. G. Infrared spectroscopy data- and physics-driven machine learning for characterizing surface microstructure of complex materials. Nat. Commun. 2020, 11, 1513

26. Hadjiivanov, K. I.; Vayssilov, G. N., Characterization of oxide surfaces and zeolites by carbon monoxide as an IR probe molecule. In Advances in Catalysis, Academic Press: 2002; Vol. 47, pp 307-511.

27. Asokan, C.; DeRita, L.; Christopher, P. Using probe molecule FTIR spectroscopy to identify and characterize Pt-group metal based single atom catalysts. Chin. J. Catal. 2017, 38, 1473-1480

28. Concepción, P.; Boronat, M.; Millán, R.; Moliner, M.; Corma, A. Identification of distinct copper species in Cu-CHA samples using NO as probe molecule. A combined IR spectroscopic and DFT study. Top. Catal. 2017, 60, 1653-1663

29. Sheppard, N.; De La Cruz, C., Vibrational spectra of hydrocarbons adsorbed on metals: Part I. Introductory principles, ethylene, and the higher acyclic alkenes. In Advances in Catalysis, Eley, D. D.; Haag, W. O.; Gates, B., Eds. Academic Press: 1996; Vol. 41, pp 1-112.

30. Trenary, M. Reflection absorption infrared spectroscopy and the structure of molecular adsorbates on metal surfaces. Annu. Rev. Phys. Chem. 2000, 51, 381-403

31. Aylor, A. W.; Lobree, L. J.; Reimer, J. A.; Bell, A. T. Investigations of the dispersion of Pd in H-ZSM-5. J. Catal. 1997, 172, 453-462

32. Chakarova, K.; Ivanova, E.; Hadjiivanov, K.; Klissurski, D.; Knözinger, H. Co-ordination chemistry of palladium cations in Pd-H-ZSM-5 as revealed by FTIR spectra of adsorbed and co-adsorbed probe molecules (CO and NO). Phys. Chem. Chem. Phys 2004, 006, 3702-3709

33. Khivantsev, K.; Jaegers, N. R.; Koleva, I. Z.; Aleksandrov, H. A.; Kovarik, L.; Engelhard, M.; Gao, F.; Wang, Y.; Vayssilov, G. N.; Szanyi, J. Stabilization of super electrophilic Pd+2 cations in small-pore SSZ-13 zeolite. J. Phys. Chem. C 2020, 124, 309-321

34. Tessier, D.; Rakai, A.; Bozon-Verduraz, F. Spectroscopic study of the interaction of carbon monoxide with cationic and metallic palladium in palladium–alumina catalysts. J. Chem. Soc., Faraday Trans. 1992, 88, 741-749

35. Juszczyk, W.; Karpiński, Z.; Ratajczykowa, I.; Stanasiuk, Z.; Zieliński, J.; Sheu, L. L.; Sachtler, W. M. H. Characterization of supported palladium catalysts: III. PdAl2O3. J. Catal. 1989, 120, 68-77

36. Vijayanand, P.; Chakarova, K.; Hadjiivanov, K.; Lukinskas, P.; Knözinger, H. On the nature of Pdn+ surface carbonyl and nitrosyl complexes formed on Pd-promoted tungstated zirconia catalyst. Phys. Chem. Chem. Phys 2003, 5, 4040-4044

37. Muravev, V.; Spezzati, G.; Su, Y.-Q.; Parastaev, A.; Chiang, F.-K.; Longo, A.; Escudero, C.; Kosinov, N.; Hensen, E. J. M. Interface dynamics of Pd–$CeO_2$ single-atom catalysts during CO oxidation. Nat. Catal. 2021, 4, 469-478

38. Spezzati, G.; Su, Y.; Hofmann, J. P.; Benavidez, A. D.; DeLaRiva, A. T.; McCabe, J.; Datye, A. K.; Hensen, E. J. M. Atomically dispersed Pd–O species on $CeO_2$(111) as highly active sites for low-temperature CO oxidation. ACS Catal. 2017, 7, 6887-6891

39. Guo, Y.; Li, Y.; Du, X.; Li, L.; Jiang, Q.; Qiao, B. Pd single-atom catalysts derived from strong metal-support interaction for selective hydrogenation of acetylene. Nano Res. 2022, 15, 10037-10043

40. Kim, Y.; Collinge, G.; Lee, M.-S.; Khivantsev, K.; Cho, S. J.; Glezakou, V.-A.; Rousseau, R.; Szanyi, J.; Kwak, J. H. Surface density dependent catalytic activity of single palladium atoms supported on ceria. Angew. Chem. Int. Ed. 2021, 60, 22769-22775

41. Liu, P.; Zhao, Y.; Qin, R.; Mo, S.; Chen, G.; Gu, L.; Chevrier, D. M.; Zhang, P.; Guo, Q.; Zang, D.; Wu, B.; Fu, G.; Zheng, N. Photochemical route for synthesizing atomically dispersed palladium catalysts. Science 2016, 352, 797-800

42. Jiang, D.; Wan, G.; Halldin Stenlid, J.; García-Vargas, C. E.; Zhang, J.; Sun, C.; Li, J.; Abild-Pedersen, F.; Tassone, C. J.; Wang, Y. Dynamic and reversible transformations of subnanometre-sized palladium on ceria for efficient methane removal. Nat. Catal. 2023, 6, 618-627

43. Xin, P.; Li, J.; Xiong, Y.; Wu, X.; Dong, J.; Chen, W.; Wang, Y.; Gu, L.; Luo, J.; Rong, H.; Chen, C.; Peng, Q.; Wang, D.; Li, Y. Revealing the active species for aerobic alcohol oxidation by using uniform supported palladium catalysts. Angew. Chem. Int. Ed. 2018, 57, 4642-4646

44. Jiang, D.; Wan, G.; García-Vargas, C. E.; Li, L.; Pereira-Hernández, X. I.; Wang, C.; Wang, Y. Elucidation of the active sites in single-atom Pd1/$CeO_2$ catalysts for low-temperature CO oxidation. ACS Catal. 2020, 10, 11356-11364

45. An, Y.; Chen, S.-Y.; Zhou, L.; Wang, B.; Hao, G.; Chen, J.; Wang, Y.; Zhang, H.; Peng, Z.; Yang, T.-C.; Yang, C.-M.; Chen, J.-L.; Tsung, C.-K.; Liu, Z.; Chou, L.-Y. Sintering resistance of Pd single atoms on steam-modified ceria: Deciphering the role of hydroxyl groups. J. Mater. Chem. A 2023, 11, 21285-21292

46. Szanyi, J.; Kwak, J. H. Dissecting the steps of CO2 reduction: 2. The interaction of CO and CO2 with Pd/γ-Al2O3: An in situ FTIR study. Phys. Chem. Chem. Phys 2014, 16, 15126-15138

47. Jiao, L.; Regalbuto, J. R. The synthesis of highly dispersed noble and base metals on silica via strong electrostatic adsorption: I. Amorphous silica. J. Catal. 2008, 260, 329-341

48. Paparazzo, E. Corrigendum: Use and mis-use of X-ray photoemission Ce3d spectra of Ce2O3 and $CeO_2$ (2018 J. Phys.: Condens. Matter 30 343003). J. Phys.: Condens. Matter. 2020, 32, 099501

49. Redhead, P. A. Thermal desorption of gases. Vacuum 1962, 12, 203-211

50. Dudarev, S. L.; Botton, G. A.; Savrasov, S. Y.; Humphreys, C. J.; Sutton, A. P. Electron-energy-loss spectra and the structural stability of nickel oxide: An LSDA+U study. Phys. Rev. B 1998, 57, 1505-1509

51. Rohrbach, A.; Hafner, J.; Kresse, G. Electronic correlation effects in transition-metal sulfides. J. Phys.: Condens. Matter. 2003, 15, 979

52. Blöchl, P. E. Projector augmented-wave method. Phys. Rev. B 1994, 50, 17953-17979

53. Kresse, G.; Joubert, D. From ultrasoft pseudopotentials to the projector augmented-wave method. Phys. Rev. B 1999, 59, 1758-1775

54. Kresse, G.; Furthmüller, J. Efficient iterative schemes for ab initio total-energy calculations using a plane-wave basis set. Phys. Rev. B 1996, 54, 11169-11186

55. Kettner, M.; Ševčíková, K.; Homola, P.; Matolín, V.; Nehasil, V. Influence of the Ce–F interaction on cerium photoelectron spectra in CeOXFY layers. Chem. Phys. Lett. 2015, 639, 126-130

56. Kettner, M.; Duchoň, T.; Wolf, M. J.; Kullgren, J.; Senanayake, S. D.; Hermansson, K.; Veltruská, K.; Nehasil, V. Anion-mediated electronic effects in reducible oxides: Tuning the valence band of ceria via fluorine doping. J. Chem. Phys. 2019, 151, 044701

57. Wolf, M. J.; Kullgren, J.; Broqvist, P.; Hermansson, K. Fluorine impurities at $CeO_2$(111): Effects on oxygen vacancy formation, molecular adsorption, and surface re-oxidation. J. Chem. Phys. 2017, 146, 044703

58. Lustemberg, P. G.; Yang, C.; Wang, Y.; Wöll, C.; Ganduglia-Pirovano, M. V. Vibrational frequencies of CO bound to all three low-index cerium oxide surfaces: A consistent theoretical description of vacancy-induced changes using density functional theory. J. Chem. Phys. 2023, 159, 034704

59. Yang, C.; Capdevila-Cortada, M.; Dong, C.; Zhou, Y.; Wang, J.; Yu, X.; Nefedov, A.; Heißler, S.; López, N.; Shen, W.; Wöll, C.; Wang, Y. Surface refaceting mechanism on cubic ceria. J. Phys. Chem. Lett. 2020, 11, 7925-7931

60. Yang, C.; Yin, L.-L.; Bebensee, F.; Buchholz, M.; Sezen, H.; Heissler, S.; Chen, J.; Nefedov, A.; Idriss, H.; Gong, X.-Q.; Wöll, C. Chemical activity of oxygen vacancies on ceria: a combined experimental and theoretical study on $CeO_2$(111). Phys. Chem. Chem. Phys 2014, 16, 24165-24168

61. Yang, C.; Yu, X.; Heißler, S.; Nefedov, A.; Colussi, S.; Llorca, J.; Trovarelli, A.; Wang, Y.; Wöll, C. Surface faceting and reconstruction of ceria nanoparticles. Angew. Chem. Int. Ed. 2017, 56, 375-379

62. Unterhalt, H.; Rupprechter, G.; Freund, H.-J. Vibrational sum frequency spectroscopy on Pd(111) and supported Pd nanoparticles: CO adsorption from ultrahigh vacuum to atmospheric pressure. J. Phys. Chem. B 2002, 106, 356-367

63. Neitzel, A.; Figueroba, A.; Lykhach, Y.; Skála, T.; Vorokhta, M.; Tsud, N.; Mehl, S.; Ševčíková, K.; Prince, K. C.; Neyman, K. M.; Matolín, V.; Libuda, J. Atomically dispersed Pd, Ni, and Pt species in ceria-based catalysts: Principal differences in stability and reactivity. J. Phys. Chem. C 2016, 120, 9852-9862

64. Figueroba, A.; Kovács, G.; Bruix, A.; Neyman, K. M. Towards stable single-atom catalysts: Strong binding of atomically dispersed transition metals on the surface of nanostructured ceria. Cat. Sci. Technol. 2016, 6, 6806-6813

65. Colussi, S.; Gayen, A.; Farnesi Camellone, M.; Boaro, M.; Llorca, J.; Fabris, S.; Trovarelli, A. Nanofaceted Pd-O sites in Pd-Ce surface superstructures: Enhanced activity in catalytic combustion of methane. Angew. Chem. Int. Ed. 2009, 48, 8481-8484

66. He, B.; Wang, J.; Ma, D.; Tian, Z.; Jiang, L.; Xu, Y.; Cheng, S. Interaction of Pd single atoms with different $CeO_2$ crystal planes: A first-principles study. Appl. Surf. Sci. 2018, 433, 1036-1048

67. Bruix, A.; Lykhach, Y.; Matolínová, I.; Neitzel, A.; Skála, T.; Tsud, N.; Vorokhta, M.; Stetsovych, V.; Ševčíková, K.; Mysliveček, J.; Fiala, R.; Václavů, M.; Prince, K. C.; Bruyère, S.; Potin, V.; Illas, F.; Matolín, V.; Libuda, J.; Neyman, K. M. Maximum Noble-Metal Efficiency in Catalytic Materials: Atomically Dispersed Surface Platinum. Angew. Chem. Int. Ed. 2014, 53, 10525-10530

68. Maurer, F.; Jelic, J.; Wang, J.; Gänzler, A.; Dolcet, P.; Wöll, C.; Wang, Y.; Studt, F.; Casapu, M.; Grunwaldt, J.-D. Tracking the formation, fate and consequence for catalytic activity of Pt single sites on $CeO_2$. Nat. Catal. 2020, 3, 824-833

69. Khivantsev, K.; Jaegers, N. R.; Aleksandrov, H. A.; Song, I.; Pereira-Hernandez, X. I.; Engelhard, M. H.; Tian, J.; Chen, L.; Motta Meira, D.; Kovarik, L.; Vayssilov, G. N.; Wang, Y.; Szanyi, J. Single Ru(II) Ions on Ceria as a Highly Active Catalyst for Abatement of NO. J. Am. Chem. Soc. 2023, 145, 5029-5040

70. Wang, J.; Sauter, E.; Nefedov, A.; Heißler, S.; Maurer, F.; Casapu, M.; Grunwaldt, J.-D.; Wang, Y.; Wöll, C. Dynamic Structural Evolution of Ceria-Supported Pt Particles: A Thorough Spectroscopic Study. J. Phys. Chem. C 2022, 126, 9051-9058

# Pacific Northwest National Laboratory

902 Battelle Boulevard
P.O. Box 999
Richland, WA 99354

1-888-375-PNNL (7665)

***www.pnnl.gov***